ACS APPLIED ELECTRONIC MATERIALS

pubs.acs.org/acsaelm

Article

Insight into the Diindolo[3,2-*b*:2′,3′-*h*]carbazole Core as an Air-Stable Semiconductor for OTFTs

Roger Bujaldón, Anna Vilche, Joaquim Puigdollers, Cristina Puigjaner, Xavier Alcobé, and Dolores Velasco*

Cite This: *ACS Appl. Electron. Mater.* 2023, 5, 3675−3684

Read Online

ACCESS | Metrics & More | Article Recommendations | Supporting Information

ABSTRACT: Encouraged by the outstanding performance of pentacene, the perspective over enhanced organic semiconductors has been focused on studying analogous ladder-type materials. In this context, the case of the diindolo[3,2-*b*:2′,3′-*h*]carbazole core is a promising example of a semiconductor with improved stability. Herein, we report the synthesis of five diindolo[3,2-*b*:2′,3′-*h*]carbazole derivatives displaying different alkylation patterning, as well as their integration in organic thin-film transistors. The elucidation of the single-crystal structures of three of the derivatives, accomplished by means of powder X-ray diffraction (PXRD), provided further insight into the intermolecular disposition of this core. As a result, the relationship between the structural design and the performance of the final devices could be analyzed. Globally, a scope of mobility values from 10^{-6} to 10^{-3} cm^2 V^{-1} s^{-1} was achieved by just fine-tuning the length of the alkyl chains and the type of passivation layer applied onto the SiO_2 surface. Remarkably, all the fabricated devices excel in terms of temporal and air stability with a shelf lifetime up to years, a coveted feature in organic electronics that confirms the potential of this core.

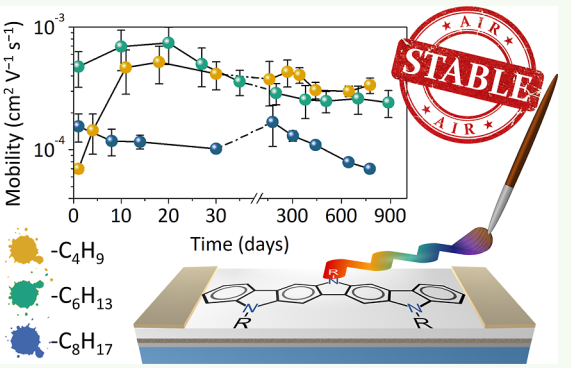

KEYWORDS: *organic electronics, OTFTs, p-type semiconductors, diindolocarbazole, ladder-type molecules, air-stable materials, PXRD*

Downloaded via 161.116.162.34 on January 16, 2025 at 17:09:05 (UTC).
See https://pubs.acs.org/sharingguidelines for options on how to legitimately share published articles.

1. INTRODUCTION

The interest in organic materials has increased considerably, just as they eventually found application in different electronic devices in front of the hitherto omnipresent inorganic materials.[1−4] Indeed, organic semiconductors offer unique and interesting properties demanded for next-generation electronic products. Their potential in flexible low-cost manufacturing and access to easily tunable electronic properties are just a few within the range of advantages.[5−7] This field, comprising both small molecules and polymers, has been extensively reviewed in devices such as organic thin-film transistors (OTFTs), organic light-emitting diodes (OLEDs), and organic photovoltaic cells (OPCs).[8−10]

A major goal nowadays is the development of air-stable materials bearing high charge mobility values. The mobility displayed by an organic semiconductor is affected by numerous factors, being the most decisive the intrinsic properties of the organic compound and its arrangement and morphology in the solid state.[10−13] The design should therefore address not only the molecular but also the supramolecular level. Extended π-conjugated systems favor stronger intermolecular interactions between adjacent molecules and thus facilitate the charge transport through the film. Large aromatic constructions built from a broad variety of building blocks have been developed so far, proving the efficacy of this strategy.[14−18]

Inspired by the excellent properties of pentacene, many efforts have been invested on studying analogue ladder-type materials that overcome its major drawbacks, namely, poor air stability and insolubility in organic solvents.[19] In this context, the diindolo[3,2-*b*:2′,3′-*h*]carbazole core (depicted in Figure 1) appears as a good candidate, mimicking the linear π-extension of pentacene while incorporating the advantages of the carbazole heterocycle. In fact, 9*H*-carbazole is a frequently resorted synthetic building block because of its easy availability and low cost, providing hole-transporting properties with stability against oxidative doping by atmospheric oxygen.[13,20] Despite the efforts put in the research of alternative ladder-type materials, the case of the diindolo[3,2-*b*:2′,3′-*h*]carbazole core still remains rather unexplored. Up to now, there are just few described synthetic approaches toward a progressively expanding set of reported derivatives.[21−25] However, to the best of our knowledge, this is the first study concerning its semiconductor properties and integration in OTFT devices.

Received: March 29, 2023
Accepted: May 17, 2023
Published: June 16, 2023

© 2023 The Authors. Published by American Chemical Society

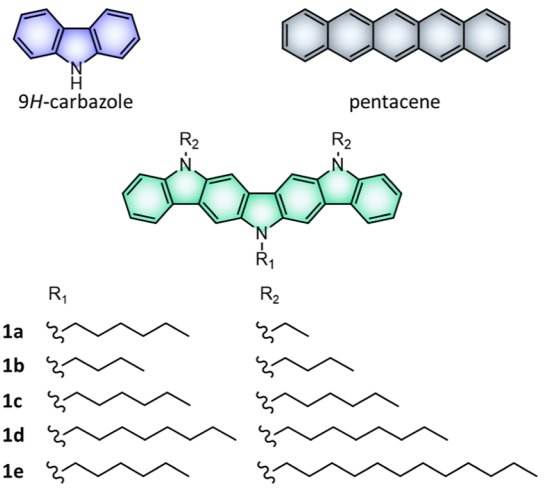

Figure 1. Chemical structures of 9*H*-carbazole, pentacene, and the set of five diindolo[3,2-*b*:2′,3′-*h*]carbazole derivatives **1a**−**e** studied in this work.

Keeping in mind the importance of the intermolecular disposition and arrangement of the organic semiconductor, herein, we considered the synthesis of derivatives featuring flexible alkyl chains with different lengths and substitution patternings. The diindolo[3,2-*b*:2′,3′-*h*]carbazole structure possesses three nitrogens that can be alkylated, offering the opportunity to improve the solubility and adjust the intermolecular arrangement without modifying the main core properties.[2,26−30] Of these, one corresponds to the central carbazole unit while the other two are situated in the peripheral indole extensions. Consequently, the system permits a homogeneous alkylation patterning, with all three alkyl chains displaying the same length, or a heterogeneous one by varying only the length of the peripheral *N*-alkyl chains. Specifically, we designed a set of five diindolo[3,2-*b*:2′,3′-*h*]carbazole derivatives: three of them display a homogeneous substitution pattern, namely, tributyl (**1b**), trihexyl (**1c**), and trioctyl (**1d**), whereas the other two maintain the hexyl chain on the central carbazole while the peripheral indoles feature either shorter ethyl (**1a**) or longer dodecyl (**1e**) chains (Figure 1). Besides the characterization of their physical properties, these derivatives have been integrated in OTFTs. Concerning the OTFT architecture, the focus has been placed on the optimization of the dielectric−semiconductor interface by comparing two different passivation layers, that is, polystyrene (PS) and octadecyltrichlorosilane (OTS). This element also plays a key role in determining the performance of the final device.[31−34] In order to get further insight into the role of these structural features and the main core design, the elucidation of the crystal structures represented a crucial step. In this context, the resolution via powder X-ray diffraction (PXRD) proved as a valuable support for the interpretation of derivatives **1a**, **1b**,[35] and **1d**, which represent the only reported crystal structures of *N*-trialkylated diindolocarbazole derivatives to date. The notorious stability of these materials as p-type semiconductors in OTFT devices, which extends to periods up to years, definitely fosters the potential of this core.

2. EXPERIMENTAL SECTION

2.1. Instrumentation and Methods. The synthetic procedure and characterization of all compounds are detailed in the Supporting Information. ^{1}H NMR spectra were acquired in a Varian Mercury instrument (400 MHz) and ^{13}C NMR in a Bruker 400 MHz Advance III instrument (100 MHz) or a Bruker Advance Neo 500 MHz instrument (125 MHz). NMR spectra were processed using the MestRec Nova software (version 14.2.0) and referenced using the solvent signal. Absorption and emission spectra were recorded in a Varian Cary UV−vis−NIR 500E spectrophotometer and a PTI fluorimeter, respectively. Fluorescence quantum yields (Φ_f) were estimated employing a reported protocol.[36] For this, 1,4-bis(5-phenyl-2-oxazolyl)benzene (POPOP) was chosen as standard (Φ_f = 0.93 in cyclohexane at a λ_{ex} = 300 nm). Cyclic voltammograms were acquired in a cylindrical three-electrode cell using a microcomputer-controlled potentiostat/galvanostat Autolab with PGSTAT30 equipment and GPES software (version 4.9). The reference was an Ag/Ag$^+$ electrode (10^{-3} M $AgNO_3$ in acetonitrile), the working electrode consisted of a glassy-carbon electrode, and the counter electrode was a platinum wire. All voltammograms were collected under quiescent conditions and under argon atmosphere at 100 mV s^{-1}. All compounds were dissolved in distilled dichloromethane (10^{-3} M) and tetrabutylammonium hexafluorophosphate (TBAP, 0.1 M) was employed as the supporting electrolyte. All potentials were referred to the Fc$^+$/Fc redox couple. The ionization potentials (IPs) were estimated from the onset of the first oxidation peak ($^{ox}E_{onset}$) as IP = $^{ox}E_{onset}$ + 5.39, where 5.39 eV corresponds to the formal potential in the Fermi scale of the Fc$^+$/Fc couple.[37] The electron affinities (EAs) were estimated as EA = IP − E_{gap}. The optical gap energies (E_{gap}) were estimated from the λ_{onset} of the absorption spectra. The thermogravimetric analyses (TGAs) and the differential scanning calorimetry (DSC) thermograms were collected at a scan rate of 10 °C min^{-1} under nitrogen atmosphere in a TA Instruments Q50 and TA Instruments Q2000 calorimeter, respectively. Powder X-ray diffraction patterns were obtained on a PANalytical X'Pert PRO MPD diffractometer of 240 mm of radius in transmission configuration, using Cu $K_{\alpha 1+2}$ radiation (λ = 1.5418 Å) with a focalizing elliptic mirror and a PIXcel detector working at a maximum detector's active length of 3.347°. Incident and diffracted beam 0.02 radians soller slits (**1a**) or 0.01 radians soller slits (**1d**) and incident beam slits defining a beam height of 0.4 mm have been used with the sample sandwiched between the films of polyester of 3.6 μm of thickness. **1a**: 48 consecutive 2θ scans were measured and added from 1 to 70° in 2θ, with a step size of 0.026° and a measuring time of 350 s per step (total measuring time 50 h). **1d**: 31 consecutive 2θ scans were measured and added from 2 to 70° in 2θ, with a step size of 0.013° and a measuring time of 350 s per step (total measuring time 64 h). Out-of-plane grazing incidence X-ray diffraction (GIXRD) measurements of thin films (75 nm thickness) were collected in a PANalytical X'Pert PRO MRD diffractometer. It incorporated a PIXcel detector, a parabolic Göbel mirror at the incident beam, and a parallel plate collimator at the diffracted beam, with Cu Kα radiation (λ = 1.5418 Å) and a work power of 45 kV × 40 mA. An optimized angle of incidence around 0.17° was used for the measurements. The morphology of the layers, analyzed by means of atomic force microscopy (AFM), was registered using an AFM Dimension 3100 system connected to a Nanoscope IVa electronics unit (Bruker).

2.2. OTFT Fabrication and Characterization. The OTFTs were constructed using a bottom-gate top-contact architecture. The substrates consisted of thermally oxidized crystalline silicon wafers with gate dielectric (SiO_2) thicknesses ranging from 115 to 135 nm. The gate side of the silicon wafer was partially treated with ammonium fluoride. The substrates were then cleaned by subsequent ultrasonic treatments in acetone, isopropanol, and water, dried using a nitrogen blow, and heated at 100 °C for 5 min. The SiO_2 surface was covered with either octadecyltrichlorosilane (OTS) or polystyrene (PS) as a passivation layer. The formation of the OTS self-assembled monolayer (SAM)[38,39] was achieved by immersing the substrates in a solution of OTS (2 mM) in toluene for 24 h at room temperature. The substrates were cleansed by subsequent ultrasonic treatments in toluene, acetone, and isopropanol and eventually dried using a nitrogen blow and heated at 100 °C for 5 min. The deposition of the PS layer was carried out using a solution of PS in toluene (4 mg mL^{-1}), which was spin-coated onto the wafer. The substrate was spun

https://doi.org/10.1021/acsaelm.3c00412
ACS Appl. Electron. Mater. 2023, 5, 3675−3684

Scheme 1. Synthetic Route Toward Compounds 1a−e[a]

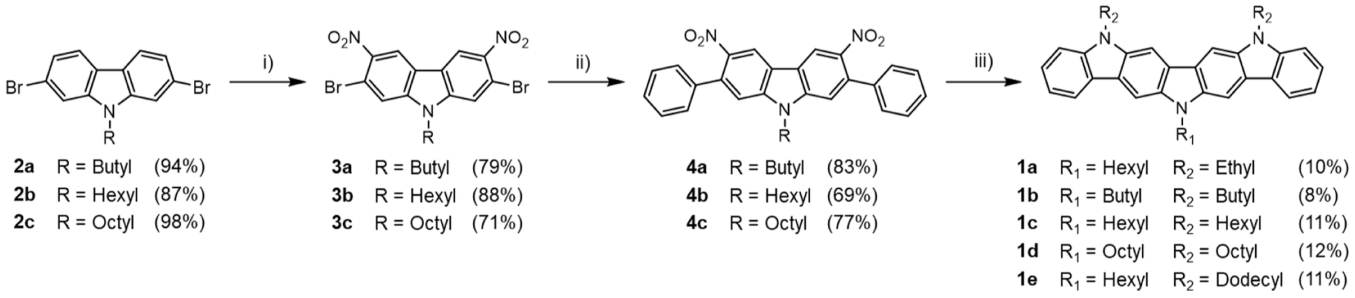

[a]Reagents and conditions: (i) HNO_3 (90%), AcOH, 100 °C; (ii) phenylboronic acid, $Pd(PPh_3)_4$, K_2CO_3, THF/H_2O, reflux; (iii) (1) $P(OEt)_3$, *o*-DCB, μW 230 °C, (2) NaH, R_2−Br, DMF, RT.

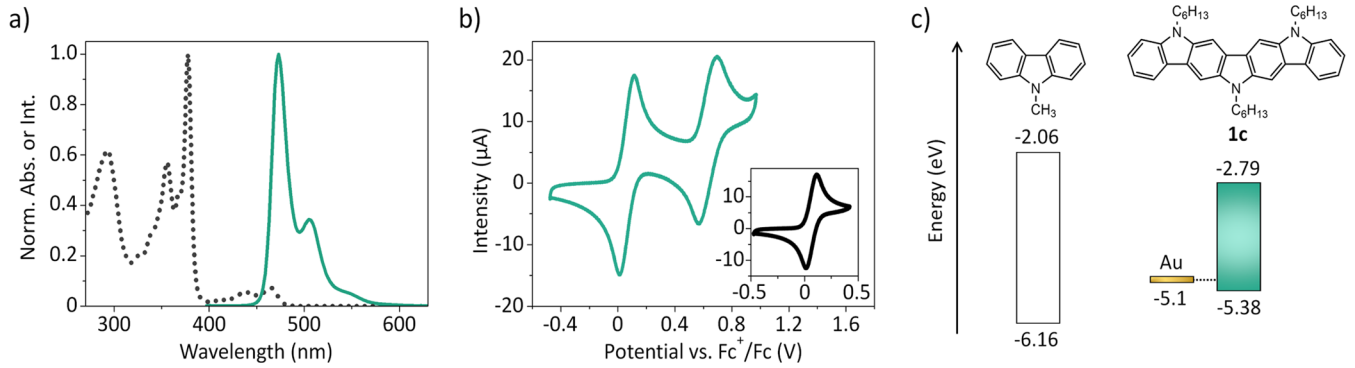

Figure 2. Photophysical and electrochemical characterization: (a) absorption (dotted) and emission (solid) spectra in dichloromethane of derivative **1c**; (b) cyclic voltammetry of derivative **1c** in dichloromethane, referred to the Fc^+/Fc redox couple (the inset shows only the first oxidation step); (c) schematic representation of the energy levels of 9-methyl-9*H*-carbazole[13] and **1c** (IP = ${}^{ox}E_{onset}$ + 5.39 and EA = IP − E_{gap}) with respect to the gold work function.

at 1500 rpm for 5 s and 2500 rpm for 33 s employing a P6700 spin-coater. The substrates were then annealed at 120 °C for 1 h. The organic compounds were deposited by thermal evaporation under vacuum in a chamber with a pressure below 10^{-6} mbar. The sublimation temperature for each compound was controlled manually to maintain the deposition at a stable rate of 0.3 Å s^{-1} until the semiconductor layers of about 75 nm thickness were obtained. The wafers were subsequently transferred to another vacuum system to deposit the gold contacts. The drain and source electrodes were defined by a shadow mask, providing a channel length and width of 80 μm and 2 mm, respectively. The resultant OTFTs were characterized under ambient conditions in the dark. The electrical characteristics were recorded employing a Keithley 2636A source meter. The charge carrier mobility was calculated in the saturation regime (μ_{sat}) from eq 1

$$I_D = \mu_{sat} C_{ox} \frac{W}{2L} (V_G - V_{th})^2 \quad (1)$$

where W and L correspond to the channel width and length, respectively, and C_{ox} is the capacitance per unit area of the gate insulator. The average hole mobility values ($\mu_{h,avg}$) and their corresponding standard deviations were calculated from an array up to eight analogous devices. All devices were stored under ambient conditions in the dark.

3. RESULTS AND DISCUSSION

3.1. Synthesis. As mentioned, there are few available synthetic procedures to construct the diindolo[3,2-*b*:2′,3′-*h*]carbazole core. The recent approach proposed by Srour et al.,[22] based on a twofold Cadogan ring closure facilitated by microwave irradiation, permits a more versatile and straightforward synthesis toward it. This route was employed to furnish the compounds **1a−e** as shown in Scheme 1. The starting materials **2a−c** were prepared by alkylating under standard conditions[40] the 2,7-dibromo-9*H*-carbazole, which was synthesized from the commercially available 4,4′-dibromobiphenyl using the reported methods.[41,42] Positions 3 and 6 of compounds **2a−c** were then nitrated to obtain **3a−c**. A twofold Suzuki−Miyaura cross-coupling reaction was carried out to anchor the phenyl moieties of compounds **4a−c**.[43] Finally, the twofold Cadogan reaction under microwave irradiation permitted the formation of the indole extensions, and the corresponding nitrogens were subsequently alkylated. Compound **4b** enabled the formation of the desired products **1a**, **1c,** and **1e**, whereas **1b** and **1d** were obtained from **4a** and **4c**, respectively. The detailed procedure can be found in the Supporting Information.

3.2. Material Characterization. The photophysical, electrochemical, and thermal properties of compounds **1a−e** have been explored. As expected, the characteristics of the diindolo[3,2-*b*:2′,3′-*h*]carbazole backbone govern the physical properties of all derivatives in solution, while the role of the *N*-alkyl chains is secondary. As representatives, the absorption and emission spectra and the cyclic voltammetry of **1c** are collected in Figure 2. The linear extension of the π-system of diindolo[3,2-*b*:2′,3′-*h*]carbazole results in a bathochromic shift of the absorption and emission spectra with respect to the carbazole ring,[13] achieving relatively low optical band gaps of ∼2.59 eV that still ameliorate the exceedingly low value of pentacene (1.85 eV).[8] The resulting emission is placed into the blue-green region, with fluorescence quantum yields up to 0.16. Compounds **1a−e** underwent two reversible oxidation

https://doi.org/10.1021/acsaelm.3c00412
ACS Appl. Electron. Mater. 2023, 5, 3675−3684

processes. Interestingly, all possess rather low onset oxidation potentials, with resulting HOMO energy levels around −5.39 eV that are appropriate for the Au work function (−5.1 eV). As a result, the estimated energy levels of this set of derivatives are perfectly suitable for their application in optoelectronic devices, particularly making them ideal for hole injection and transport, while also promoting a substantially long-term stability.[22]

Concerning their thermal properties, all derivatives presented good thermal stability with decomposition temperatures (T_d) higher than 320 °C, which are convenient for their vacuum deposition. In this case, the T_d (corresponding to the 5% weight loss obtained from TGA) is certainly conditioned by the length of the *N*-alkyl chains, being the most stable those derivatives with longer alkyl chains. Their melting temperatures (T_m) follow the opposite tendency, with the values from 268 to 111 °C corresponding to the derivatives **1a** and **1e**, respectively. A more detailed compilation of the photophysical, electrochemical, and thermal characterization can be found in Table S1 of the Supporting Information.

3.3. Organic Thin-Film Transistors. The diindolo[3,2-*b*:2′,3′-*h*]carbazole derivatives **1a−e** were investigated and characterized as p-type semiconductors in OTFTs. They were tested as vacuum-deposited active layers (75 nm of thickness) in standard bottom gate-top contact devices using gold as the source and drain electrodes. The effect of two distinct passivation layers recovering the SiO_2 surface, namely, octadecyltrichlorosilane (OTS) and polystyrene (PS), was also investigated. Also, each set of devices was measured periodically to characterize the evolution of the charge mobility over time. Table 1 compiles the data of OTFTs based on the compounds **1a−e** in OTS- and PS-treated devices and Figure 3 illustrates the characteristics of **1b,d** over OTS as representatives.

Specifically, Table 1 contains the maximum mobility obtained for a specific device ($\mu_{h,max}$) and the maximum average mobility obtained for a set of analogous devices on a day ($\mu_{h,avg}$). Additionally, the average mobility of the set after approximately a year is also collected to evaluate the air and temporal stability. Globally, the obtained hole mobility values cover ca. three orders of magnitude, from 10^{-6} to 10^{-3} cm^2 V^{-1} s^{-1}, depending on the alkylation patterning and the nature of the interfacial dielectric. In particular, the highest mobility values were extracted with the tributylated **1b** and the trihexylated **1c**, both featuring relatively short and homogeneous *N*-alkyl chains. Regarding the passivation layer, PS-treated devices clearly outpace their OTS- counterparts for all compounds except for the tributylated derivative **1b**. In fact, **1b** displayed the highest mobility of all OTS-treated devices with a value of 1.1×10^{-3} cm^2 V^{-1} s^{-1}, whereas it was slightly lower over PS, that is, 6.7×10^{-4} cm^2 V^{-1} s^{-1}. The OTFT characteristics of the former are represented in Figure 3a,b.

Table 1. OTFT Hole Mobilities of a Set of Representative Devices Based on Compounds 1a−e in OTS- and PS-Treated Substrates, Corresponding to the Maximum Value Obtained for a Single Device and the Average Mobility of a Set of Devices

	SiO_2/OTS		SiO_2/PS	
	$\mu_{h,max}$[a] (cm^2 V^{-1} s^{-1})	$\mu_{h,avg}$[b] (cm^2 V^{-1} s^{-1})	$\mu_{h,max}$[a] (cm^2 V^{-1} s^{-1})	$\mu_{h,avg}$[b] (cm^2 V^{-1} s^{-1})
1a	7.8×10^{-5}	6×10^{-5} (6×10^{-5})	1.5×10^{-4}	1×10^{-4} (8×10^{-5})
1b	1.1×10^{-3}	8×10^{-4} (4×10^{-4})	6.7×10^{-4}	5×10^{-4} (3×10^{-4})
1c	1.7×10^{-4}	1×10^{-4} (9×10^{-5})	1.1×10^{-3}	8×10^{-4} (3×10^{-4})
1d	6.3×10^{-5}	6×10^{-5} (2×10^{-5})	2.1×10^{-4}	2×10^{-4} (1×10^{-4})
1e	6.3×10^{-6}	5×10^{-6} (—)[c]	4.9×10^{-5}	4×10^{-5} (—)[c]

[a]Maximum hole mobility value for a single device. [b]Average hole mobility collected on the day with the maximum value, corresponding to a set of representative devices. The values in parenthesis correspond to the average mobility registered after a year. [c]Not measured.

Derivative **1c** also outstands with an analogous $\mu_{h,max}$ of 1.1×10^{-3} cm^2 V^{-1} s^{-1}, which in this case was registered over PS. The further elongation of the *N*-alkyl chains translates into a descend of the hole mobility, especially over OTS. Overall, the aliphatic nature of OTS is generally detrimental for this core, a trend that is reversed only by mitigating the presence of the *N*-alkyl chains.

The most remarkable feature of this core resides in the notorious air and temporal stability displayed by all devices, with a shelf lifetime up to years maintaining a considerably uniform $\mu_{h,avg}$ over time. This prominent asset represents a permanently sought-after characteristic in OTFTs. Indeed, well-known organic semiconductors such as pentacene or TIPS-pentacene fall behind in terms of stability even considering amending strategies such as encapsulation.[44]

The analyzed structural factors, that is, the *N*-alkylation patterning or the passivation treatment, modulate the performance of the devices without discrediting their shelf lifetime. Figure 4 represents the evolution of the $\mu_{h,avg}$ over time of the homogeneously substituted derivatives **1b−1d**. As observed, devices fabricated over OTS tend to show their maximum charge mobility values during the first days after fabrication with a moderate decline over time. On the other hand, the charge mobility values on their PS counterparts reach their maximum several weeks after their fabrication, stabilizing thereafter in a plateau. Also, the choice of PS implies a superior long-term uniformity of the $\mu_{h,avg}$ and more robustness in front of the *N*-alkylation patterning.

The heterogeneous alkylation patterning of compounds **1a** and **1e** clearly causes a decrease of the device performance with respect to the homogeneous **1c**, which also features a central *N*-hexyl chain. The shortening of the peripheral chains to ethyl in **1a** derives into a substantial decrease of the $\mu_{h,max}$ up to an order of magnitude in PS-treated devices. The underperformance becomes even more remarkable with the elongation of the peripheral chains to dodecyl in **1e**, inducing a 20-fold drop over both passivation layers. The evolution of their average hole mobilities is shown in Figure S1 of the Supporting Information.

In general, all devices show a slight sublinear behavior that accentuates into a hump-like nonlinearity over time. This phenomenon was suggested to originate from gated Schottky contacts.[45] Accordingly, the mobility values have been extracted from the higher V_G region.[45−47] Another feature of the studied devices that should be pointed out is the relatively low I_{on}/I_{off} ratios they display. Seemingly, those compounds featuring longer alkyl chains, namely, **1d** and **1e**, show the highest I_{on}/I_{off} ratios with values up to 10^3 and a more defined off state (~10^{-11} A) in the absence of V_G (Figure 3c,d illustrates the characteristics of **1d** as representative). This tendency was already observed on similar studies concerning

https://doi.org/10.1021/acsaelm.3c00412
ACS Appl. Electron. Mater. 2023, 5, 3675−3684

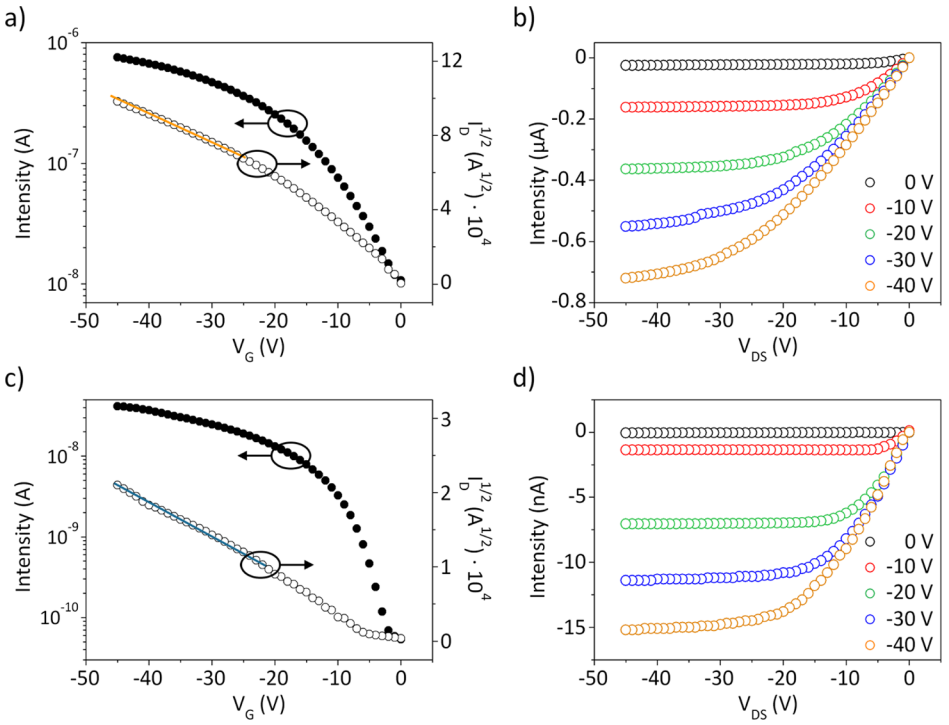

Figure 3. OTFT characteristics of representative OTS-treated devices fabricated with **1b** (a,b) and **1d** (c,d): transfer (V_{DS} = −40 V) and saturation characteristics of **1b** (a) and **1d** (c); output characterization at different gate voltages of **1b** (b) and **1d** (d). The measurements correspond to the first day after fabrication.

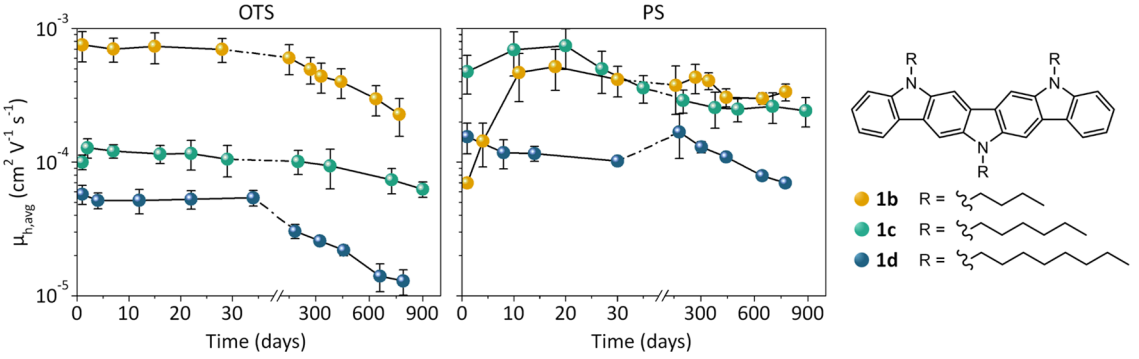

Figure 4. Evolution profile of the average hole mobility ($\mu_{h,avg}$) of a set of devices fabricated from compounds **1b** (orange), **1c** (green), and **1d** (blue) over OTS (left) and PS (right). The displayed period comprises 900 days starting from the fabrication day.

different aromatic cores.[29,48] A more detailed representation of the OTFT characteristics of devices containing derivatives **1a**−**e** is shown in Figures S2−S12 of the Supporting Information.

Overall, the *N*-alkylation patterning exerts a great impact on the hole mobility beyond the main diindolocarbazole backbone. Thus, the fine-tuning of the *N*-alkyl chains length alongside the appropriate interfacial passivation layer is required to extract the full potential of this core. In this way, the trend observed for compounds **1a**−**e** indicates a prominent outperformance of derivatives displaying short and homogeneous *N*-alkyl chains.

3.4. Solid-State Disposition within the Film. The next step comprises the correlation of the charge mobility results acquired from the OTFT devices with the structural design of the diindolocarbazole derivatives. For this purpose, the crystallographic characterization of the synthesized derivatives represented an essential information. Even after considerable attempts regarding all derivatives, however, we could not produce single crystals with the required size and quality to determine their crystal structures and define their molecular dispositions. Consequently, we attempted the elucidation of their crystal structures from powder X-ray diffraction (PXRD). Indeed, this approach was confirmed as a convenient procedure for determining the crystal structure of the tributylated derivative **1b**.[35] On the basis of these initial results, the aforementioned protocol also succeeded in the elucidation of two additional structures, that is, derivatives **1a** and **1d**. The powder X-ray diffractogram of **1a** was perfectly indexed to an orthorhombic unit cell with unit cell parameters a = 48.56 Å, b = 42.90 Å, and c = 5.23 Å and a volume of 10890 Å^3, after excluding three little reflections that were attributed to an impurity. On the other hand, the powder X-ray diffractogram of **1d** was indexed to a monoclinic unit cell with unit cell parameters a = 24.21 Å, b = 4.84 Å, c = 34.87 Å, and β = 97.7° and a volume of 4050 Å^3. Taking into account the unit cell volume, the molecular weight of each compound, and an

https://doi.org/10.1021/acsaelm.3c00412
ACS Appl. Electron. Mater. 2023, 5, 3675−3684

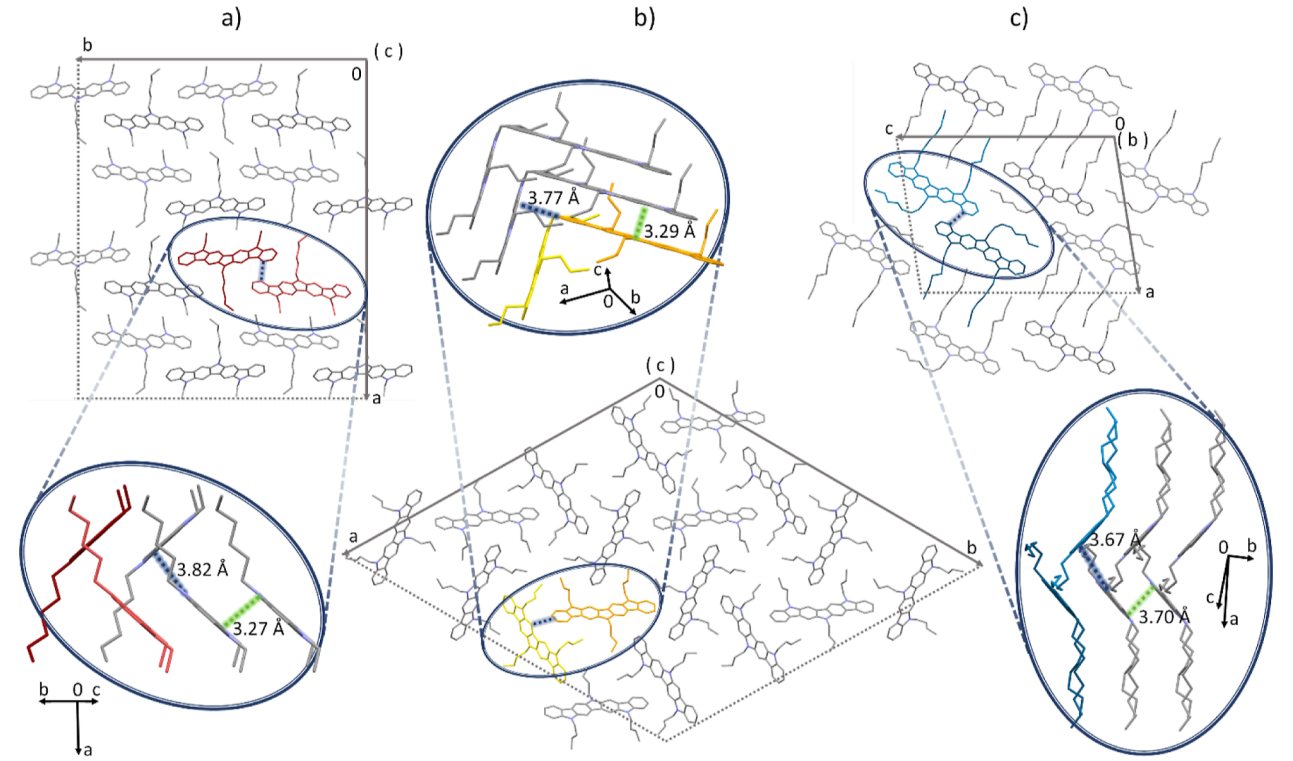

Figure 5. Single-crystal structures of derivatives: (a) **1a**, (b) **1b**, and (c) **1d**, with the cell axes delimiting the unit cells. The amplified regions indicate the $\pi-\pi$ stacking distances in green (3.27 and 3.29 Å through the *c* axis in **1a** and **1b**, respectively, and 3.70 Å through the *b* axis in **1d**) and the edge-to-face C−H···π distances in blue.

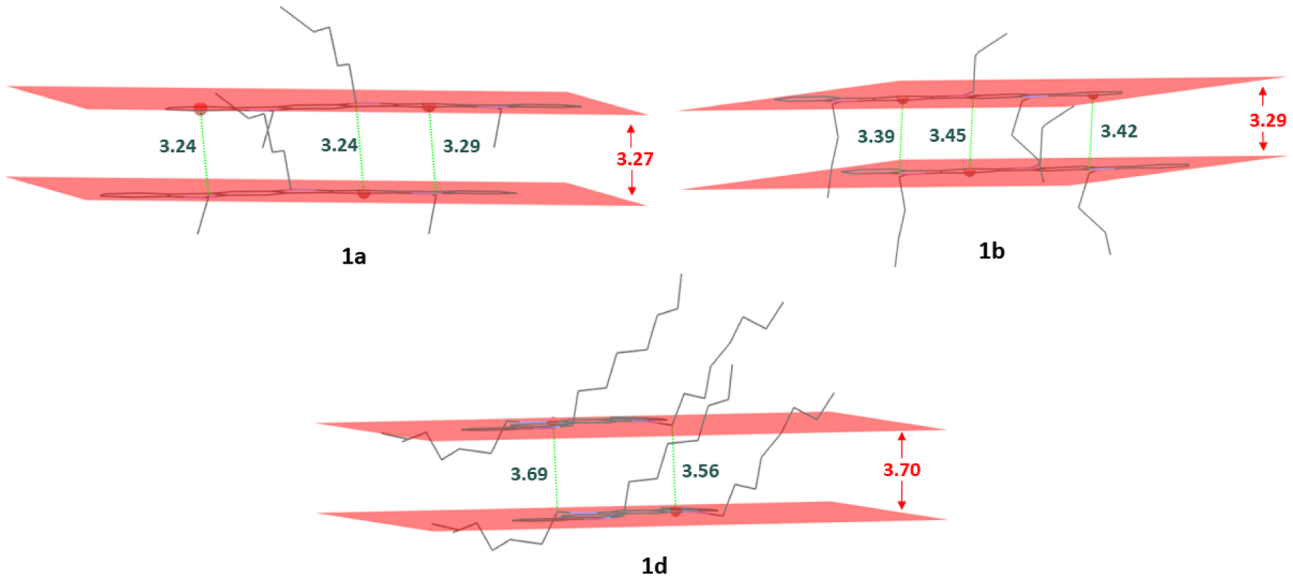

Figure 6. Strong $\pi-\pi$ parallel-displaced stackings (shortest intermolecular $\pi-\pi$ distances (Å) in red) and C−H···π interactions (C···centroid distances (Å) in green) between parallel molecules of **1a**, **1b**, and **1d**.

estimated density value of 1.2 Mg/m^3, the number of molecules in the unit cell was calculated to be $Z = 16$ for **1a** and $Z = 4$ for **1d**. The space groups *Fdd*2 and $P2_1/c$ were assigned for **1a** and **1d**, respectively, based on the systematic absences. Moreover, the subsequent Pawley pattern matchings fitted very well the experimental X-ray powder diffractograms in both cases, being the agreement factors 2.80% (**1a**) and 1.30% (**1d**) (Figure S13, Supporting Information). Their crystal structures were solved by using the global optimization simulated annealing approach integrated in TOPAS, and a starting model of each compound was obtained after optimization with the program SPARTAN. Some constraints were introduced, considering the molecules as rigid bodies using the *Z*-matrix notation, which was allowed to rotate and translate in the three directions within the unit cell. Planar restrictions were applied to the aromatic rings and several torsion angles of the flexible aliphatic chains were refined (7 in **1a** and 21 in **1d**). Chemical sense solutions with agreement factors of 15.3% (**1a**) and 10.3% (**1d**) were obtained. The crystal structures were subsequently refined by the Rietveld

https://doi.org/10.1021/acsaelm.3c00412
ACS Appl. Electron. Mater. 2023, 5, 3675−3684

method also by means of TOPAS v6 software, giving satisfying results with low R_{wp} values (**1a**: 5.16%, **1d**: 2.55%) (Figure S14, Supporting Information).

The elucidated crystal structures of **1a**, **1b**, and **1d** are depicted in Figure 5, whereas the most relevant parameters for the determinations and refinements are summarized in Table S2 of the Supporting Information. Their crystal structures, although belonging to different crystal systems, have in common two long unit cell parameters (of ca. 35−53 Å) and a shorter one of about 5 Å, which is the one related to the $\pi-\pi$ stacking interactions. In fact, all three systems arrange atop each other in a slipped parallel disposition due to the planarity of their π-conjugated system, granting the intermolecular overlapping that is sought in organic electronics. This packing can be associated with a convenient γ type, which is mainly governed by face-to-face C···C (and C···N in this case) interactions between parallel translated molecules with the support of edge-to-face C−H···π interactions.[49,50] As highlighted in Figure 5, the $\pi-\pi$ stacking distances are as short as 3.27 and 3.29 Å in **1a** and **1b**, respectively, which agree with an effective charge transport through the film. In the case of the trioctylated **1d**, this distance is increased to a less favorable value of 3.70 Å that could justify the lower mobility values collected in OTFTs with respect to the other homogeneously *N*-alkylated derivatives. The edge-to-face C−H···π interactions are also close (3.82, 3.77, and 3.67 Å for **1a**, **1b**, and **1d**, respectively), endowing the materials with a potential alternative mechanism for the charge transport. The offset lateral displacements in **1a**, **1b**, and **1d** are 4.08, 4.23, and 3.12 Å, respectively.

Regarding the role of the *N*-alkylation in the intermolecular arrangement, **1a** and **1b** show the same C−H···π interactions between the alkyl chains (all three methylene groups adjacent to the N atoms) and the aromatic systems of contiguous diindolocarbazole molecules along the *c* axis, reinforcing the packing in this direction (Figure 6). Contrarily, in the case of **1d**, only two of the three alkyl chains participate in these interactions, being the distances longer than the previous ones. Also, the superior length of the octyl chains emphasizes the presence of aliphatic-predominating regions in the unit cell, which could explain the higher I_{on}/I_{off} ratios found in the corresponding devices.[29,48]

The solid-state characterization of the semiconductor layers was achieved by means of grazing incidence X-ray diffraction (GIXRD). The measurements were performed on vacuum-evaporated films of 75 nm of thickness over OTS- and PS-treated Si/SiO_2 substrates, equivalent to the active layers of the devices. The GIXRD patterns of derivatives **1a**−**d** are shown in Figure 7.

In the cases of **1a**, **1b** and **1d**, the availability of their single crystal structures enabled the indexation of the GIXRD patterns. The diffraction peaks at 2θ = 7.0 and 13.9° observed in the **1a** films were suggested as the reflections 400 and 800, respectively, on the basis of the powder pattern diffractogram and the crystal structure. In the case of **1b**, the principal diffraction signal peaking at 2θ = 7.2° was proposed to belong to the reflection 4−20, whereas the main peak of **1d** at 2θ = 5.1° was assigned to the reflection 002. This is sign that the reflections 400, 4−20, and 002 in **1a**, **1b**, and **1d**, respectively, are arranged parallel to the substrate as schematized in Figure 8. Consequently, the $\pi-\pi$ stacking directions, which coincide with the *c* axis in structures **1a**−**b** and the *b* axis in **1d**, are also parallel to the substrate. The signals of **1b** peaking at 2θ = 8.9

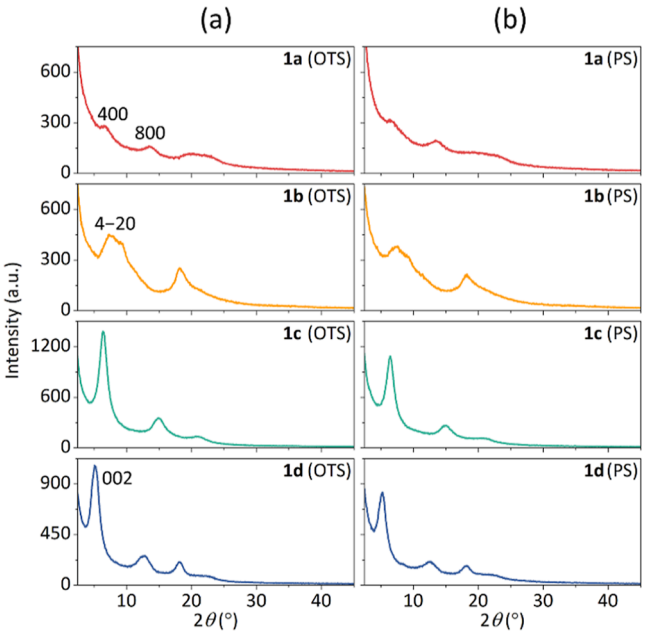

Figure 7. Analysis of the solid-state organization: GIXRD patterns corresponding to thin films (75 nm of thickness) of compounds **1a**−**d** deposited under vacuum over OTS- (a) and PS-treated (b) substrates.

and 18.0° were suggested as the reflections 5−40 and 10−80. In the case of **1d**, peaks at 2θ = 12.7° and 18.0° were instead proposed as reflections 302 and 206, respectively. It should be noted that, even in the case of a polymorphic layer, all the proposed reflections preserve a parallel $\pi-\pi$ stacking direction with respect to the substrate. The underperformance of the heterogeneous derivative **1a** as semiconductor could be associated with the highly disordered or amorphous arrangement within the films, as confirmed by the exceedingly low degree of order they exhibit. The proposed arrangements in the thin films of all three compounds, especially considering the adaptability and multiple hopping pathways of a γ motif, admit a proper charge transport through the semiconductor layers.

The morphology of the thin films was inspected by means of atomic force microscopy (AFM). Compound **1c** exhibited conveniently uniform films over PS, whereas the presence of localized protrusions when deposited over OTS slightly increased the roughness. The same trend was detected for **1d**, so these differences agree with the outperformance of their PS-treated devices. On the contrary, **1b**-based were hampered by a more spiked morphology that was not conditioned by the passivation layer. Therefore, the GIXRD and AFM data suggest that the already superior performance of **1b** could be further improved by optimizing the deposition conditions in subsequent studies. The AFM images of films based on the derivatives **1b**−**d** over OTS- and PS-treated substrates are collected in the Supporting Information (Figures S15−S17).

The nature of the passivation layer certainly influences the morphology of the thin films but, according to the GIXRD patterns, the effect over the supramolecular order is not substantial. Another plausible hypothesis of the diverging mobilities between OTS- and PS-treated devices could be associated with the arrangement within the semiconductor/dielectric interface, that is, the first molecular layers that are deposited, rather than in the main bulk.[51−53] Previous density functional theory (DFT) calculations performed with the

https://doi.org/10.1021/acsaelm.3c00412
ACS Appl. Electron. Mater. 2023, 5, 3675−3684

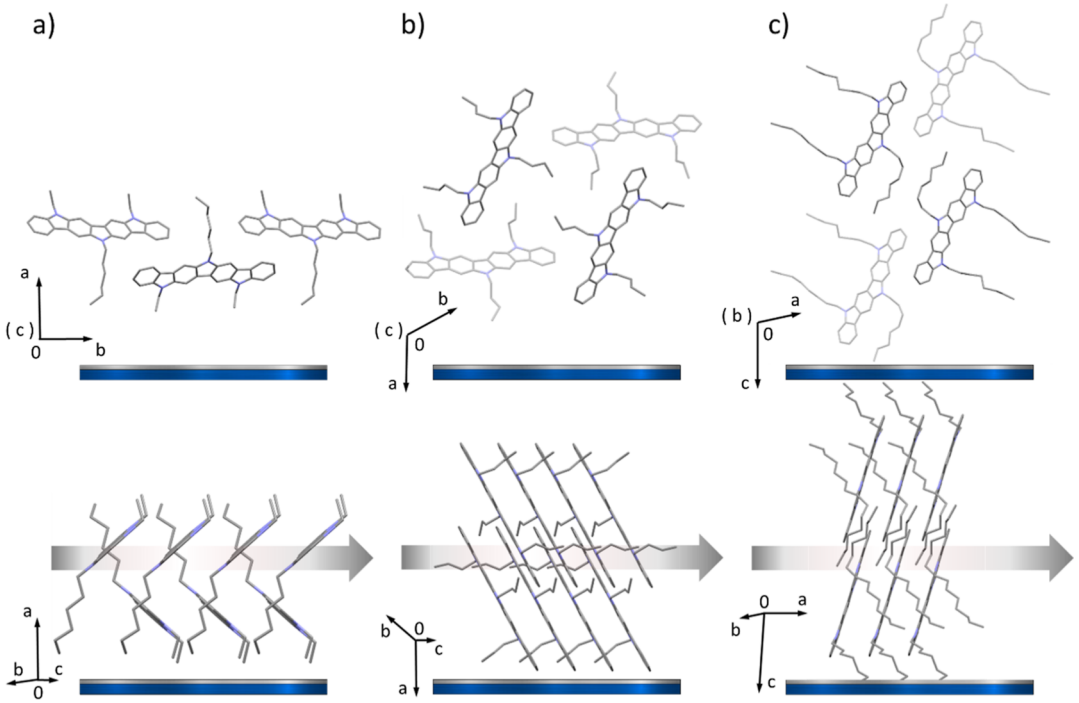

Figure 8. Proposed disposition of **1a** (a), **1b** (b), and **1d** (c) in the thin film from two different perspectives, in accordance with the main reflections observed in the GIXRD pattern. The reflections 400, 4−20, and 002 are placed parallel to the substrate for **1a**, **1b**, and **1d**, respectively. The $\pi-\pi$ stacking directions, which are parallel to the substrate, are also indicated. The molecular dispositions depicted for **1a** and **1b** correspond to representative fragments of the unit cells. Hydrogen atoms have been omitted for clarity.

regioisomer diindolo[3,2-*a*:3′,2′-*c*]carbazole already shed light on how the length of the *N*-alkyl chains can affect the interactions of the system with the dielectric depending on the passivation layer, as reported by our research group.[29] Similar to the herein presented results, the *N*-hexylated diindolo[3,2-*a*:3′,2′-*c*]carbazole displayed higher mobility values over PS-treated devices. This was attributed to the stabilized edge alkyl···PS interactions, which favor an edge-to-face disposition (π-stacking direction parallel to the substrate) on the interface that is analogous to that of the bulk. Contrarily, the same system is connected to OTS via weakly hydrophobic London dispersion alkyl−H···π and alkyl···alkyl, but the associated interaction energy is much lower than with PS. Consequently, the arrangement in that case presented a less ordered disposition in the interface, deriving into lower mobility values over OTS-treated devices. This trend is reversed with the reduction of the *N*-alkyl chain length in the same degree as the series **1b−d**. DFT calculations established that, in the presence of shorter *N*-alkyl chains, the system can only establish π···PS interactions, inducing a disadvantageous face-on disposition to the first-deposited molecular layers over PS that is not detected over OTS. Once again, these results highlight the special care needed at designing the structure of the semiconductor material.

4. CONCLUSIONS

Herein, we synthesized a set of five diindolo[3,2-*b*:2′,3′-*h*]carbazole derivatives displaying *N*-alkyl chains with various lengths and patterns. All of them presented adequate photophysical and electrochemical properties for their application as p-type semiconductors. The reported hole mobility values, ranging from 10^{-6} to 10^{-3} cm^2 V^{-1} s^{-1}, are highly dependent on the *N*-alkylation design and the passivation layer applied onto the SiO_2/semiconductor interface. Remarkably, a hole mobility as high as 1.1×10^{-3} cm^2 V^{-1} s^{-1} was achieved with the tributylated **1b** over OTS-based devices and the trihexylated **1c** over PS ones. The crystal structures, elucidated via PXRD, revealed a convenient γ packing that is accordant with the favorable device performances. In fact, the crystallographic study in conjunction with the GIXRD measures of the thin films shed light on the role of the structural design in modulating the device performance. The relationship between the structural variations and the charge mobility values also reveals an appealing outperformance of derivatives possessing short and homogeneous *N*-alkyl chains. Overall, the diindolocarbazole core claims a great potential as a hole-transporting semiconductor, supported by its noteworthy air stability and shelf lifetime in OTFT devices, which extends to periods up to several years. Even considering the outperforming characteristics of state-of-the-art devices, these initial results could be further improved by tailoring the deposition conditions or engineering the different interfaces. This study should therefore usher in the optimization and implementation of this core in organic electronics.

■ ASSOCIATED CONTENT

Supporting Information

The Supporting Information is available free of charge at https://pubs.acs.org/doi/10.1021/acsaelm.3c00412.

Synthesis and characterization, OTFT characterization, elucidation process of the crystal structures, crystallographic data, and AFM imaging (PDF)

https://doi.org/10.1021/acsaelm.3c00412
ACS Appl. Electron. Mater. 2023, 5, 3675−3684

AUTHOR INFORMATION

Corresponding Author

Dolores Velasco − *Grup de Materials Orgànics, Institut de Nanociència i Nanotecnologia (IN2UB), Departament de Química Inorgànica i Orgànica, Secció de Química Orgànica, Universitat de Barcelona, E-08028 Barcelona, Spain;* orcid.org/0000-0002-9357-5860; Email: dvelasco@ub.edu

Authors

Roger Bujaldón − *Grup de Materials Orgànics, Institut de Nanociència i Nanotecnologia (IN2UB), Departament de Química Inorgànica i Orgànica, Secció de Química Orgànica, Universitat de Barcelona, E-08028 Barcelona, Spain*

Anna Vilche − *X-ray Diffraction Unit, Scientific and Technological Centers, University of Barcelona, E-08028 Barcelona, Spain*

Joaquim Puigdollers − *Dept. Enginyeria Electrònica, Universitat Politècnica de Catalunya, E-08034 Barcelona, Spain;* orcid.org/0000-0002-1834-2565

Cristina Puigjaner − *X-ray Diffraction Unit, Scientific and Technological Centers, University of Barcelona, E-08028 Barcelona, Spain*

Xavier Alcobé − *X-ray Diffraction Unit, Scientific and Technological Centers, University of Barcelona, E-08028 Barcelona, Spain*

Complete contact information is available at: https://pubs.acs.org/10.1021/acsaelm.3c00412

Author Contributions

The manuscript was written through the contributions of all authors. All authors have given approval to the final version of the manuscript.

Funding

This research was funded by the Ministerio de Economía, Indústria y Competitividad (grant number FUNMAT-PGC2018-095477-B-I00).

Notes

The authors declare no competing financial interest.

ACKNOWLEDGMENTS

The authors want to thank Josep M. Bassas (XRD unit) and Jordi Díaz and Aránzazu Villuendas (Nanometric Techniques Unit) of the CCiTUB for the assistance with the GIXRD measurements and the AFM measures, respectively. Also, they want to thank Gisela Bujaldón for the help with the graphic design. R.B. acknowledges the grant FI AGAUR from Generalitat de Catalunya.

REFERENCES

(1) Wang, C.; Dong, H.; Jiang, L.; Hu, W. Organic semiconductor crystals. *Chem. Soc. Rev.* **2018**, *47*, 422−500.

(2) Khatun, M. N.; Dey, A.; Meher, N.; Iyer, P. K. Long Alkyl Chain Induced OFET Characteristic with Low Threshold Voltage in an n-Type Perylene Monoimide Semiconductor. *ACS Appl. Electron. Mater.* **2021**, *3*, 3575−3587.

(3) Jia, X.; Fuentes-Hernandez, C.; Wang, C.-Y.; Park, Y.; Kippelen, B. Stable organic thin-film transistors. *Sci. Adv.* **2018**, *4*, No. eaao1705.

(4) Vahland, J.; Leo, K.; Kleemann, H. Quasi-Self-Aligned Organic Thin-Film Transistors in Coplanar Top-Gate Configuration. *ACS Appl. Electron. Mater.* **2021**, *3*, 5131−5137.

(5) Bronstein, H.; Nielsen, C. B.; Schroeder, B. C.; McCulloch, I. The role of chemical design in the performance of organic semiconductors. *Nat. Rev. Chem.* **2020**, *4*, 66−77.

(6) Feng, L.; Tang, W.; Zhao, J.; Yang, R.; Hu, W.; Li, Q.; Wang, R.; Guo, X. Unencapsulated Air-stable Organic Field Effect Transistor by All Solution Processes for Low Power Vapor Sensing. *Sci. Rep.* **2016**, *6*, 20671.

(7) Ros, E.; Reig, M.; Voz, C.; Bagdziunas, G.; Ortega, P.; Velasco, D.; Puigdollers, J. Shedding Light on the Negative Differential Resistance Effect Observed in Organic Thin-Film Transistors. *ACS Appl. Electron. Mater.* **2020**, *2*, 1574−1582.

(8) Jiang, W.; Li, Y.; Wang, Z. Heteroarenes as high performance organic semiconductors. *Chem. Soc. Rev.* **2013**, *42*, 6113−6127.

(9) Maria Angela, V.; Anjali, A.; Harshini, D.; Nagarajan, S. Organic Light-Emitting Transistors: From Understanding to Molecular Design and Architecture. *ACS Appl. Electron. Mater.* **2021**, *3*, 550−573.

(10) Ueberricke, L.; Mastalerz, M. Triptycene End-Capping as Strategy in Materials Chemistry to Control Crystal Packing and Increase Solubility. *Chem. Rec.* **2021**, *21*, 558−573.

(11) Liao, H.; Chen, M.; Sun, J.; Haseena, S.; Ravva, M. K.; Xiao, C.; Zhang, L.; Wang, Y.; Li, Z.; Yue, W. Novel and asymmetric S,N-heterocyclics with fused six-membered rings for organic field effect transistor applications. *J. Mater. Chem. C* **2020**, *8*, 17083−17089.

(12) He, K.; Li, W.; Tian, H.; Zhang, J.; Yan, D.; Geng, Y.; Wang, F. Asymmetric Conjugated Molecules Based on [1]Benzothieno[3,2-b][1]benzothiophene for High-Mobility Organic Thin-Film Transistors: Influence of Alkyl Chain Length. *ACS Appl. Mater. Interfaces* **2017**, *9*, 35427−35436.

(13) Reig, M.; Puigdollers, J.; Velasco, D. Molecular order of air-stable p-type organic thin-film transistors by tuning the extension of the π-conjugated core: The cases of indolo[3,2-b]carbazole and triindole semiconductors. *J. Mater. Chem. C* **2015**, *3*, 506−513.

(14) Chen, J.; Yang, K.; Zhou, X.; Guo, X. Ladder-Type Heteroarene-Based Organic Semiconductors. *Chem.−Asian J.* **2018**, *13*, 2587−2600.

(15) Takimiya, K.; Shinamura, S.; Osaka, I.; Miyazaki, E. Thienoacene-Based Organic Semiconductors. *Adv. Mater.* **2011**, *23*, 4347−4370.

(16) Cai, Z.; Awais, M. A.; Zhang, N.; Yu, L. Exploration of Syntheses and Functions of Higher Ladder-type π-Conjugated Heteroacenes. *Chem* **2018**, *4*, 2538−2570.

(17) Niimi, K.; Shinamura, S.; Osaka, I.; Miyazaki, E.; Takimiya, K. Dianthra[2,3-*b*:2′,3′-*f*]thieno[3,2-*b*]thiophene (DATT): Synthesis, Characterization, and FET Characteristics of New π-Extended Heteroarene with Eight Fused Aromatic Rings. *J. Am. Chem. Soc.* **2011**, *133*, 8732−8739.

(18) Grimsdale, A. C.; Müllen, K. Oligomers and Polymers Based on Bridged Phenylenes as Electronic Materials. *Macromol. Rapid Commun.* **2007**, *28*, 1676−1702.

(19) Tang, M. L.; Okamoto, T.; Bao, Z. High-Performance Organic Semiconductors: Asymmetric Linear Acenes Containing Sulphur. *J. Am. Chem. Soc.* **2006**, *128*, 16002−16003.

(20) Ong, B. S.; Wu, Y. W.; Li, Y. Organic Semiconductors Based on Polythiophene and Indolo[3,2-*b*]carbazole. In *Organic Electronics: Materials, Manufacturing and Applications*; Klauk, H., Ed.; WILEY-VCH: Weinheim, 2006; pp 75−107. DOI: 10.1002/3527608753.ch4.

(21) Kawano, S.; Kato, M.; Soumiya, S.; Nakaya, M.; Onoe, J.; Tanaka, K. Columnar Liquid Crystals from a Giant Macrocycle Mesogen. *Angew. Chem., Int. Ed.* **2018**, *57*, 167−171.

(22) Srour, H.; Doan, T.-H.; Silva, E. D.; Whitby, R. J.; Witulski, B. Synthesis and molecular properties of methoxysubstituted diindolo-[3,2-*b*:2′,3′-*h*]carbazoles for organic electronics obtained by a consecutive twofold Suzuki and twofold Cadogan reaction. *J. Mater. Chem. C* **2016**, *4*, 6270−6279.

(23) Blouin, N.; Michaud, A.; Wakim, S.; Boudreault, P.-L. T.; Leclerc, M.; Vercelli, B.; Zecchin, S.; Zotti, G. Optical, Electrochemical, Magnetic, and Conductive Properties of New Polyindolocarbazoles and Polydiindolocarbazoles. *Macromol. Chem. Phys.* **2006**, *207*, 166−174.

(24) Wakim, S.; Bouchard, J.; Blouin, N.; Michaud, A.; Leclerc, M. Synthesis of Diindolocarbazoles by Ullmann Reaction: A Rapid Route to Ladder Oligo(p-aniline)s. *Org. Lett.* **2004**, *6*, 3413−3416.
(25) Bouchard, J.; Wakim, S.; Leclerc, M. Synthesis of Diindolocarbazoles by Cadogan Reaction: Route to Ladder Oligo-(*p*-aniline)s. *J. Org. Chem.* **2004**, *69*, 5705−5711.
(26) Lei, T.; Wang, J.-Y.; Pei, J. Roles of Flexible Chains in Organic Semiconducting Materials. *Chem. Mater.* **2014**, *26*, 594−603.
(27) Shao, J.; Zhang, X.; Tian, H.; Geng, Y.; Wang, F. Donor−acceptor−donor conjugated oligomers based on isoindigo and anthra[1,2-*b*]thieno[2,3-*d*]thiophene for organic thin-film transistors: the effect of the alkyl side chain length on semiconducting properties. *J. Mater. Chem. C* **2015**, *3*, 7567−7574.
(28) Bujaldón, R.; Peřinka, N.; Reig, M.; Cuadrado, A.; Fabregat, C.; Font-Bardía, M.; Martínez-Ferrero, E.; Velasco, D. Exploring the 3-(phenylethynyl)-9*H*-carbazole unit in the search of deep-blue emitting fluorophores. *Opt. Mater.* **2021**, *111*, 110696.
(29) Reig, M.; Bagdziunas, G.; Ramanavicius, A.; Puigdollers, J.; Velasco, D. Interface engineering and solid-state organization for triindole-based p-type organic thin-film transistors. *Phys. Chem. Chem. Phys.* **2018**, *20*, 17889−17898.
(30) Mišicák, R.; Novota, M.; Weis, M.; Cigáň, M.; Šiffalovič, P.; Nádaždy, P.; Kožíšek, J.; Kožíšková, J.; Pavúk, M.; Putala, M. Effect of alkyl side chains on properties and organic transistor performance of 2,6-bis(2,2′-bithiophen-5-yl)naphthalene. *Synth. Met.* **2017**, *233*, 1−14.
(31) Singh, M.; Kaur, N.; Comini, E. The role of self-assembled monolayers in electronic devices. *J. Mater. Chem. C* **2020**, *8*, 3938−3955.
(32) Bujaldón, R.; Puigdollers, J.; Velasco, D. Towards the bisbenzothienocarbazole core: a route of sulfurated carbazole derivatives with assorted optoelectronic properties and applications. *Materials* **2021**, *14*, 3487.
(33) Hasan, M. M.; Islam, M. M.; Li, X.; He, M.; Manley, R.; Chang, J.; Zhelev, N.; Mehrotra, K.; Jang, J. Interface Engineering With Polystyrene for High-Performance, Low-Voltage Driven Organic Thin Film Transistor. *IEEE Trans. Electron Devices* **2020**, *67*, 1751−1756.
(34) Feriancová, L.; Kmentová, I.; Micjan, M.; Pavúk, M.; Weis, M.; Putala, M. Synthesis and Effect of the Structure of Bithienyl-Terminated Surfactants for Dielectric Layer Modification in Organic Transistor. *Materials* **2021**, *14*, 6345.
(35) Vilche, A.; Bujaldón, R.; Alcobe, X.; Velasco, D.; Puigjaner, C. PXRD as a powerful tool to exploit in organic electronics: shedding light on the first *N,N′,N″*-trialkyldiindolocarbazole crystal structure. *Acta Crystallogr.* **2022**, *78*, 253−260.
(36) Crosby, G. A.; Demas, J. N. Measurement of photoluminescence quantum yields. Review. *J. Phys. Chem.* **1971**, *75*, 991−1024.
(37) Cardona, C. M.; Li, W.; Kaifer, A. E.; Stockdale, D.; Bazan, G. C. Electrochemical Considerations for Determining Absolute Frontier Orbital Energy Levels of Conjugated Polymers for Solar Cell Applications. *Adv. Mater.* **2011**, *23*, 2367−2371.
(38) Ghalgaoui, A.; Shimizu, R.; Hosseinpour, S.; Álvarez-Asencio, R.; McKee, C.; Johnson, C. M.; Rutland, M. W. Monolayer Study by VSFS: In Situ Response to Compression and Shear in a Contact. *Langmuir* **2014**, *30*, 3075−3085.
(39) Song, D.; Wang, H.; Zhu, F.; Yang, J.; Tian, H.; Geng, Y.; Yan, D. Phthalocyanato Tin(IV) Dichloride: An Air-Stable, High-Performance, n-Type Organic Semiconductor with a High Field-Effect Electron Mobility. *Adv. Mater.* **2008**, *20*, 2142−2144.
(40) Reig, M.; Gozálvez, C.; Bujaldón, R.; Bagdziunas, G.; Ivaniuk, K.; Kostiv, N.; Volyniuk, D.; Grazulevicius, J. V.; Velasco, D. Easy accessible blue luminescent carbazole-based materials for organic light-emitting diodes. *Dyes Pigm.* **2017**, *137*, 24−35.
(41) Müllen, K.; Dierschke, F.; Grimsdale, A. C. Efficient Synthesis of 2,7-Dibromocarbazoles as Components for Electroactive Materials. *Synthesis* **2003**, *2003*, 2470−2472.
(42) Freeman, A. W.; Urvoy, M.; Criswell, M. E. Triphenylphosphine-Mediated Reductive Cyclization of 2-Nitrobiphenyls: A Practical and Convenient Synthesis of Carbazoles. *J. Org. Chem.* **2005**, *70*, 5014−5019.
(43) Miyaura, N.; Suzuki, A. Palladium-Catalyzed Cross-Coupling Reactions of Organoboron Compounds. *Chem. Rev.* **1995**, *95*, 2457−2483.
(44) Chen, X.; Wang, Z.; Qi, J.; Hu, Y.; Huang, Y.; Sun, S.; Sun, Y.; Gong, W.; Luo, L.; Zhang, L.; Du, H.; Hu, X.; Han, C.; Li, J.; Ji, D.; Li, L.; Hu, W. Balancing the film strain of organic semiconductors for ultrastable organic transistors with a five-year lifetime. *Nat. Commun.* **2022**, *13*, 1480.
(45) Choi, H. H.; Cho, K.; Frisbie, C. D.; Sirringhaus, H.; Podzorov, V. Critical assessment of charge mobility extraction in FETs. *Nat. Mater.* **2018**, *17*, 2−7.
(46) Bittle, E. G.; Basham, J. I.; Jackson, T. N.; Jurchescu, O. D.; Gundlach, D. J. Mobility overestimation due to gated contacts in organic field-effect transistors. *Nat. Commun.* **2016**, *7*, 10908.
(47) McCulloch, I.; Salleo, A.; Chabinyc, M. Avoid the kinks when measuring mobility. *Science* **2016**, *352*, 1521−1522.
(48) Reig, M.; Puigdollers, J.; Velasco, D. Solid-state organization of n-type carbazole-based semiconductors for organic thin-film transistors. *Phys. Chem. Chem. Phys.* **2018**, *20*, 1142−1149.
(49) Campbell, J. E.; Yang, J.; Day, G. M. Predicted energy−structure−function maps for the evaluation of small molecule organic semiconductors. *J. Mater. Chem. C* **2017**, *5*, 7574−7584.
(50) Desiraju, G. R.; Gavezzotti, A. Crystal structures of polynuclear aromatic hydrocarbons. Classification, rationalization and prediction from molecular structure. *Acta Crystallogr.* **1989**, *45*, 473−482.
(51) Mas-Torrent, M.; Rovira, C. Role of Molecular Order and Solid-State Structure in Organic Field-Effect Transistors. *Chem. Rev.* **2011**, *111*, 4833−4856.
(52) Liu, D.; Miao, Q. Recent progress in interface engineering of organic thin film transistors with self-assembled monolayers. *Mater. Chem. Front.* **2018**, *2*, 11−21.
(53) Dinelli, F.; Murgia, M.; Levy, P.; Cavallini, M.; Biscarini, F.; de Leeuw, D. M. Spatially Correlated Charge Transport in Organic Thin Film Transistors. *Phys. Rev. Lett.* **2004**, *92*, 116802.

https://doi.org/10.1021/acsaelm.3c00412
ACS Appl. Electron. Mater. 2023, 5, 3675−3684